Quantitative phase imaging based on motionless optical scanning holography

Yoneda, Naru
Matoba, Osamu
Saita, Yusuke
Nomura, Takanori

(Citation)
Optics Letters,48(20):5273-5276

(Issue Date)
2023-10-15

(Resource Type)
journal article

(Version)
Version of Record

Optics Letters

Quantitative phase imaging based on motionless optical scanning holography

Naru Yoneda,[1,2,*] Osamu Matoba,[1,2] Yusuke Saita,[3] and Takanori Nomura[3]

[1]Graduate School of System Informatics, Department of System Science, Kobe University, Rokkodai 1-1, Nada, Kobe, 657-8501, Japan
[2]Center for Optical Scattering Image Science, Kobe University, Rokkodai 1-1, Nada, Kobe 657-8501, Japan
[3]Faculty of Systems Engineering, Wakayama University, 930 Sakaedani, Wakayama, 640-8510, Japan
*yoneda.naru@port.kobe-u.ac.jp

Received 1 June 2023; revised 10 September 2023; accepted 10 September 2023; posted 11 September 2023; published 4 October 2023

Optical scanning holography (OSH) can be applied to 3D fluorescent imaging. However, the optical setup for OSH is complicated due to the requirement of a phase shifter, a 2D mechanical scanner, and an interferometer. Although motionless optical scanning holography (MOSH) can overcome the problem, quantitative phase imaging (QPI) has not yet been realized because MOSH can only obtain incoherent holograms. If QPI in MOSH is realized, MOSH can be applied to various applications. In this Letter, MOSH-based QPI (MOSH-QPI) is proposed. In addition, a simple description of a coherent mode of OSH is presented. In the proof-of-principle experiment, the spatially divided phase-shifting technique is applied to reduce the number of measurements. The feasibility of MOSH-QPI is confirmed by measuring a phase distribution of a microlens array. MOSH-QPI is also applied to measure practical samples, and its results are compared with the experimental results of the conventional one using a Mach–Zehnder interferometer.

https://doi.org/10.1364/OL.496419

Due to the absence of an imaging lens, single-pixel imaging (SPI) [1–3] can be applied to various applications, which are impossible with a classical camera system such as imaging through scattering media [4,5]. There is a variety of SPI techniques, which are classified according to illumination patterns. Optical scanning holography (OSH) is one of the SPI techniques for using Fresnel zone patterns (FZPs) as the illumination ones [6,7]. In contrast to other SPI techniques, OSH can provide three-dimensional (3D) imaging owing to the use of FZPs. OSH has been applied for various applications such as fluorescence imaging [8], super-resolution imaging [9], multi-wavelength imaging [10], stereo imaging [11], and imaging through scattering media [12]. However, an optical setup for OSH is complicated and bulky due to the requirements of a Mach–Zehnder interferometer, a phase shifter, and a two-dimensional (2D) scanner. In order to overcome the problem, various common-path configurations have been proposed [13,14]. Particularly, motionless optical scanning holography (MOSH) simultaneously realizes the interferometer, phase shifter, and 2D scanner by using the birefringence of a liquid crystal-type spatial light modulator (SLM) [15,16]. MOSH is tolerant of vibration and environmental noise because of its common-path optical setup. There are some applications of MOSH such as fluorescence imaging [15], polarization imaging [17], and imaging through scattering media [12]; however, quantitative phase imaging (QPI) has never been proposed in MOSH. QPI is a technology that can measure nanometer-order changes, which have various informative physical quantities, such as the refractive index, thickness [18], dry mass [19], disorder strength [20], shear stress [21], aberrations [22], molecular vibration [23], and orbital angular momentum [24]. For this reason, the realization of QPI can expand the applicability of MOSH. In this Letter, MOSH-based QPI (MOSH-QPI) is proposed. Although the basic principle of MOSH-QPI is based on the coherent mode of OSH [25], the optical setup for MOSH-QPI is simple and robust to environmental disturbance owing to the common-path configuration. MOSH-QPI, therefore, overcomes the drawbacks of the coherent mode of OSH. In the field of QPI techniques, many methods have been proposed, which can be categorized as interferometric or noninterferometric. Although there are many noninterferometric QPI techniques such as Fourier ptycography and phase recovery from defocused intensity images, these methods require a mechanical scanning process to get the phase distributions. In addition, some approximation and/or huge iteration processes are also required. The proposed method can be considered as an interferometric SPI technique. While the general QPI technique uses an image sensor [26], the proposed technique is SPI, which enables phase measurement in applications where SPI is effective, such as imaging with invisible wavelength light. Compared to other common-path single-pixel phase imaging techniques [27–29], OSH uses the lateral shift of FZPs, thus eliminating the need for SLM in the pixel structure, and is compatible with FZP masks in the x-ray field. Although the proposed method uses an SLM for the FZP, this idea can be applied to various wavelength fields by fabricating an FZP mask and laterally shifting that mask while keeping the common-path configuration. As a disadvantage of OSH, the reconstructed image is affected by a PSF determined by the parameters of FZP.

A schematic of MOSH-QPI is shown in Fig. 1. A linearly

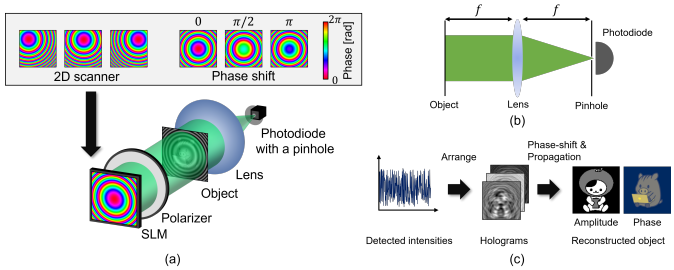

Fig. 1. Schematic of MOSH-QPI. (a) Typical optical setup for MOSH. (b) Relationship of an object plane, a lens, and a photodiode with a pinhole. (c) Reconstruction process of MOSH-QPI.

polarized plane wave illuminates a liquid crystal-type SLM. The incident beam is divided by the birefringence of the SLM. When the SLM modulates the vertical component, the reflected beam immediately in front of the SLM is described as follows:

$$u_\phi(\boldsymbol{r}) = A_x\hat{\mathbf{x}} + A_y \exp\left\{\frac{ik\boldsymbol{r}^2}{2z_r} + \phi\right\}\hat{\mathbf{y}}, \tag{1}$$

where k denotes the wavenumber and A_x and A_y denote the horizontal and vertical components, respectively. A_x and A_y can be adjusted by rotating a half-wave plate in front of the SLM. $\boldsymbol{r}$ and ϕ are the 2D coordinates at the SLM plane (x, y) and the bias phase, respectively. $\hat{\mathbf{x}}$ and $\hat{\mathbf{y}}$ are unit vectors along the horizontal and vertical directions, respectively. This beam is projected to an object plane with a 4-f optical setup through a polarizer whose polarization axis is rotated 45 degrees. A complex amplitude distribution immediately behind the object plane is described as follows:

$$u_\phi(\boldsymbol{r}') = o(\boldsymbol{r}')\left\{A_x + A_y \exp\left\{\frac{ik\boldsymbol{r}'^2}{2z_r} + \phi\right\}\right\}\frac{(\hat{\mathbf{x}} + \hat{\mathbf{y}})}{\sqrt{2}}, \tag{2}$$

where $\boldsymbol{r}'$ and $o(\boldsymbol{r}')$ are the 2D coordinates at the object plane and the complex amplitude distribution of the object. This beam is Fourier transformed by a lens and is detected by a photodiode with a pinhole. The pinhole extracts the DC component of the Fourier spectrum. The detected intensity is described as follows:

$$\begin{aligned} I_\phi &= |U_\phi(0)|^2 \\ &= \left|\int u_\phi(\boldsymbol{r}')\exp\{-i2\pi\boldsymbol{r}'\boldsymbol{v}\}\, d\boldsymbol{r}'\right|_{\boldsymbol{v}=0}^2 \\ &= \left|\int u_\phi(\boldsymbol{r}')d\boldsymbol{r}'\right|^2 \\ &= \frac{1}{2}\left|\int o(\boldsymbol{r}')\left\{A_x + A_y\exp\left\{\frac{ik\boldsymbol{r}'^2}{2z_r} + \phi\right\}\right\}d\boldsymbol{r}'\right|^2, \end{aligned} \tag{3}$$

where $\boldsymbol{v}$ is a 2D coordinate at a Fourier plane and $U_\phi(\boldsymbol{v})$ is a Fourier transform of $u_\phi(\boldsymbol{r}')$. The intensity values are sequentially detected by changing the center position of the spherical phase distribution by an SLM. By arranging the detected intensities to synchronize the center position of the spherical phase distribution, the obtained intensity distribution can be described as follows:

$$\begin{aligned} I_\phi(\boldsymbol{r}'') &= \frac{1}{2}\left|\int o(\boldsymbol{r}'')\left\{A_x + A_y\exp\left\{\frac{ik(\boldsymbol{r}'' - \boldsymbol{r}')^2}{2z_r} + \phi\right\}\right\}d\boldsymbol{r}''\right|^2 \\ &= \frac{1}{2}\left|R + o(\boldsymbol{r}'') * A_y\exp\left\{\frac{ik(\boldsymbol{r}'')^2}{2z_r} + \phi\right\}\right|^2, \end{aligned} \tag{4}$$

where $\boldsymbol{r}''$ is a 2D coordinate at a hologram plane and $*$ is a 2D convolution operator. In Eq. (4), $R = A_x\int o(\boldsymbol{r}'')d\boldsymbol{r}''$ is a constant complex value decided by an object. When R is considered as a reference beam, Eq. (4) is the same as the description of the coherent hologram, which is the same hologram as when a laser is used. In the practical case, R contains a zero-order light from an SLM. Usually, the zero-order light from an SLM is a problem in some applications. In contrast, we use zero-order light for the reference signal at the pinhole plane. Through the four-step phase-shifting method, the obtained complex amplitude distribution is described as follows:

$$\begin{aligned} u_{z_r}(\boldsymbol{r}'') &= \frac{I_0(\boldsymbol{r}'') - I_\pi(\boldsymbol{r}'') + i\left\{I_{\frac{\pi}{2}}(\boldsymbol{r}'') - I_{\frac{3\pi}{2}}(\boldsymbol{r}'')\right\}}{4} \\ &\propto o(\boldsymbol{r}'') * \exp\left\{\frac{ik(\boldsymbol{r}'')^2}{2z_r}\right\}. \end{aligned} \tag{5}$$

From Eq. (5), the complex amplitude distribution of the object is obtained by applying Fresnel backpropagation with $-z_r$. The complex amplitude distribution at the object plane can be described as follows:

$$\begin{aligned} u_0(\boldsymbol{r}'') &= o(\boldsymbol{r}'') * \exp\left\{\frac{ik(\boldsymbol{r}'')^2}{2z_r}\right\} * \exp\left\{\frac{-ik(\boldsymbol{r}'')^2}{2z_r}\right\} \\ &= o(\boldsymbol{r}'') * \mathrm{PSF}(\boldsymbol{r}''), \end{aligned} \tag{6}$$

where $\mathrm{PSF}(\boldsymbol{r}'')$ is the point spread function determined by the curvature of the spherical phase distribution. From Eq. (6), the complex amplitude distribution of the object can be obtained. Therefore, the phase distribution of the object can be measured. Note that the reconstructed complex amplitude distribution in the original MOSH is described as follows:

$$u_{\mathrm{in}}(\boldsymbol{r}'') = |o(\boldsymbol{r}'')|^2 * \mathrm{PSF}(\boldsymbol{r}''). \tag{7}$$

The derivation of Eq. (7) can be seen in Ref. [16]. By comparing Eqs. (6) and (7), although the conventional MOSH cannot get quantitative phase induced by an object, the MOSH-QPI can get the complex amplitude distribution of the object.

A proof-of-principle experiment was demonstrated to confirm the feasibility of the proposed method. The optical setup and the parameters are shown in Fig. 2. The light source is a green fiber laser (MPB Communications, Inc., VFL-P-500). The collimated beam through a spatial filter illuminates an SLM (Hamamatsu Photonics K.K. X13138-01). The center region of the SLM with 128×128 is used for displaying the spherical phase distributions. $-z_r$ of the spherical phase distribution is set to 60 mm. In this condition, the spherical phase distribution at the SLM plane does not satisfy the sampling requirement to record high spatial frequency information. The relationship between the curvature

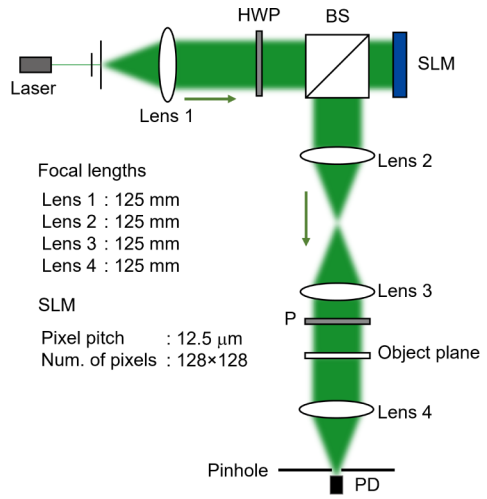

Fig. 2. Optical setup for MOSH-QPI. HWP, half-wave plate; BS, beam splitter; P, polarizer; PD, photodiode.

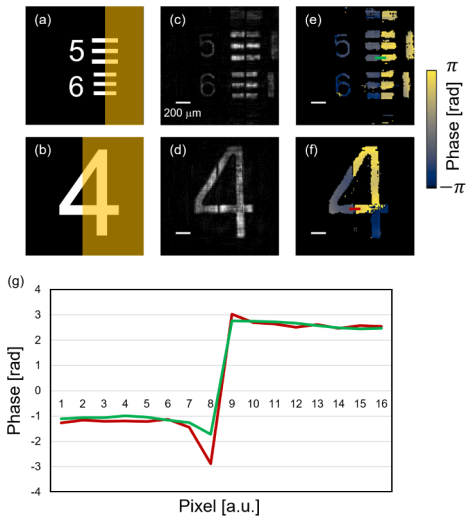

Fig. 3. Experimental results: (a) and (b) are the target objects, (c) and (d) are the reconstructed intensity distributions, (e) and (f) are the reconstructed phase distributions, and (g) is the sectional profile of green and red lines in (e) and (f).

of the spherical phase distribution and the image quality has been discussed in Ref. [16]. Since the number of pixels is 128×128 and the spatially divided phase-shifting method [16] is used, the number of measurements is $128 \times 128 = 16384$. The light from the SLM is projected to an object with a 4-f optical setup composed of lenses 2 and 3. The transmitted beam is Fourier transformed by lens 4 and is detected by a single-pixel detector composed of a pinhole (Thorlabs, Inc., P40D) and a photodiode (Hamamatsu K.K. C10439-03). The measured signals were quantized by a 16-bit analog-to-digital converter (Hamamatsu K.K. C10475). The sampling speed is limited up to 20 Hz due to the sampling rate of the analog-to-digital converter. In this experiment, the sampling rate is set to 5 Hz to reduce the noise. The measurement time is 54.6 min because 128×128 patterns are projected at 5 Hz. The diameter of the pinhole is 40 μm, which is determined by the numerical aperture of the lens 4 ($\frac{\lambda}{2\text{N.A.}} = 41.6\mu\text{m}$).

In the first experiment, the USAF test chart as an amplitude mask and a cover glass as a phase object are used. To measure the quantitative phase difference, two amplitude masks are used as shown in Figs. 3(a) and 3(b). The highlighted regions with yellow in Figs. 3(a) and 3(b) indicate the region of the cover glass. The amplitude masks in Figs. 3(a) and 3(b) are groups 2 and 0, respectively. The experimentally reconstructed complex amplitude distributions are shown in Figs. 3(c)–3(f). The results of intensity distributions in Figs. 3(c) and 3(d) indicate that the focused images can be successfully obtained from holograms. The gap regions between air and glass can also be seen from Figs. 3(c) and 3(d). Figures 3(e) and 3(f) are the results of phase distributions, which indicate that MOSH-QPI successfully measures the phase difference between air and glass. To quantitatively evaluate the phase difference, the sectional profiles at the green and red lines in Figs. 3(e) and 3(f) are extracted as shown in Fig. 3(g). The sectional profiles are mean values of 5 lines around the green and red lines. Although the phase error between the green and red lines is higher in the boundary region due to the absence of amplitude, the phase difference in the planer regions is almost the same, which indicates the proposed method can quantitatively measure the phase distribution. Notably, the optical path difference (OPD) cannot be measured by the proposed method because the thickness of the cover glass is 0.12–0.17 mm which is larger than the wavelength. To measure the OPD precisely, some phase unwrapping methods are required.

A microlens (Thorlabs, Inc., MLA150-7AR-M) array is measured by the proposed method for a practical application. The lens pitch is 150 μm and the focal length of the microlens is 5.6 mm. In this experiment, 8×8 microlenses are measured. The reconstructed phase distribution is shown in Fig. 4(a). Figures 4(b) and 4(c) are magnified microlens and theoretical phase distribution of the microlens with the experimental condition. The sectional profile of the black solid line is shown in Fig. 4(b), and the theoretical one in Fig. 4(d). These sectional profiles indicate the proposed method accurately measures the phase of the microlens. Spot intensity distribution can be obtained as shown in Fig. 4(e) by calculating the optical propagation of the complex amplitude of the result of the microlens array with a propagation distance of the focal length. The result in Fig. 4(e) indicates that phase distributions of other microlenses are also correctly measured by MOSH-QPI. These results indicate the applicability of MOSH-QPI for practical applications.

Next, we apply MOSH-QPI for the more complicated practical object. The microdot lens as shown in Fig. 5 (a) is used for this experiment and has been also used for other QPI techniques for the test as well [30–32]. The microdot lens has dot structures on its globally curved surface. The phase distribution of the lens is measured using a Mach–Zehnder interferometer for reference as shown in Fig. 5(b). The dots and the gap region can be seen in Fig. 5(b). The result of MOSH-QPI is shown in Fig. 5(c). From Fig. 5(c) an almost the same structure as Fig. 5 (b) can be measured, which indicates MOSH-QPI can be applied to practical applications. The sectional profiles at solid and dashed lines in Figs. 5(b) and 5(c) are shown in Figs. 5(d) and 5(e). The bias phase in Fig. 5(b) is adjusted for comparison. However, the results of MOSH-QPI contain low-frequency phase distribution that is caused by the aberration of the optical setup. From the sectional profiles, the relative phase differences between the outside and inside of the dot are about 1 radian. These results indicate that MOSH-QPI can measure the phase difference between dot and gap regions accurately similar to a conventional Mach–Zehnder interferometer.

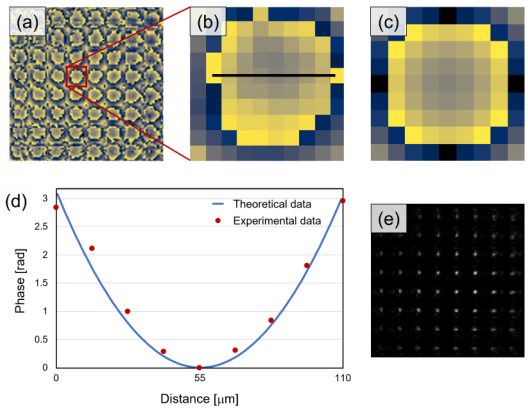

Fig. 4. Experimental results of a microlens array, (a) phase distribution, (b) enlarged microlens, (c) theoretical microlens, (d) comparison of sectional profiles, and (e) a reconstructed spot intensity distribution.

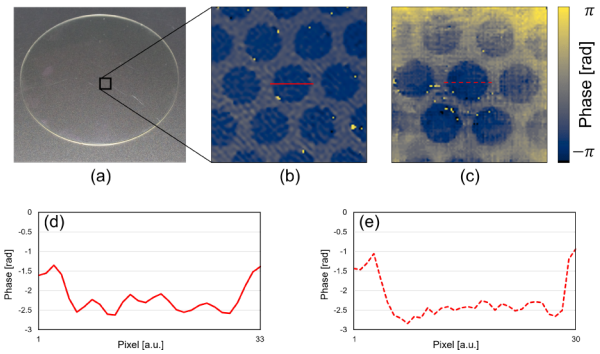

Fig. 5. Experimental results of the microdot lens (a) target and phase distributions obtained by (b) a Mach–Zehnder interferometer and (c) MOSH-QPI. (d) and (e) are sectional profiles of solid and dashed red lines in (b) and (c).

Finally, we discuss the effect of the pinhole size. Although previous research, known as partially coherent OSH, evaluates the effect of the pinhole size [33,34], it is only the effect of the intensity. So we evaluate the effect of the phase in this Letter. A Siemens star shown in Fig. 6 is used as a pure phase object in this simulation. The phase difference of the star is set to $\pi/2$. The pixel pitch Δx and the number of pixels $N \times N$ are 12.5μm and 128×128. For the pinhole, β pixels are used, and the values of β are shown in the caption of Fig. 6. From Fig. 6, the quality of the phase distribution is gradually degraded as the size of the pinhole increases. In the optical experiment, the width of the DC component is determined by a numerical aperture of a Fourier transform lens. Therefore, the pinhole size has to be precisely determined by the numerical aperture of the lens according to Eq. (3).

In this Letter, MOSH-QPI was proposed to measure the phase distribution by OSH using a simple setup. By changing the detection setup, MOSH can obtain a hologram, which is based on the coherent mode of OSH. The simple description of the coherent mode of OSH was described as Eq. (3). The experimental results indicated that MOSH-QPI can measure the phase distribution quantitatively. As a result, MOSH-QPI can be applied to various applications such as digital phase conjugation and wavefront sensing, among others.

Funding. Japan Society for the Promotion of Science (20H05886, 21H04663, 23K13680).

Disclosures. The authors declare no conflicts of interest.

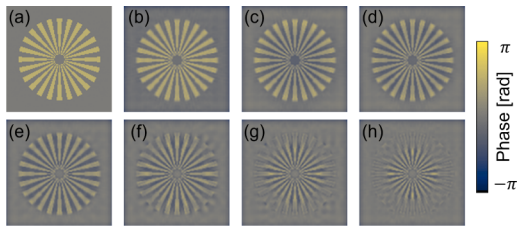

Fig. 6. Simulation results. (a) Target phase. (b)–(h) Reconstructed phase distributions when $\beta = 1, 4, 8, 12, 16, 20, 24, 28$.

Data availability. The data that support the findings of this paper are available from the corresponding author upon reasonable request.

REFERENCES

1. W. K. Pratt, J. Kane, and H. C. Andrews, Proc. IEEE **57**, 58 (1969).
2. J. H. Shapiro, Phys. Rev. A **78**, 061802 (2008).
3. Z. Zhang, X. Ma, and J. Zhong, Nat. Commun. **6**, 6225 (2015).
4. E. Tajahuerce, V. Durán, P. Clemente, E. Irles, F. Soldevila, P. Andrés, and J. Lancis, Opt. Express **22**, 16945 (2014).
5. A. J. M. Lenz, P. Clemente, V. Climent, J. Lancis, and E. Tajahuerce, Opt. Lett. **44**, 4797 (2019).
6. T. C. Poon and A. Korpel, Opt. Lett. **4**, 317 (1979).
7. T.-C. Poon, in *Optical Scanning Holography with MATLAB* (Springer, 2007).
8. B. W. Schilling, T.-C. Poon, G. Indebetouw, B. Storrie, K. Shinoda, Y. Suzuki, and M. H. Wu, Opt. Lett. **22**, 1506 (1997).
9. Z. Ren and E. Y. Lam, Proc. SPIE **10022**, 1002203 (2016).
10. H. Kim, Y. S. Kim, and T. Kim, Appl. Opt. **55**, A17 (2016).
11. J.-P. Liu and S.-Y. Wang, IEEE Trans. Ind. Inf. **12**, 1664 (2016).
12. N. Yoneda, Y. Saita, and T. Nomura, Appl. Phys. Lett. **119**, 161101 (2021).
13. T. Kim and T. Kim, Opt. Lett. **45**, 2046 (2020).
14. J.-P. Liu, C.-M. Tsai, T.-C. Poon, P. Tsang, and Y. Zhang, Opt. Lasers Eng. **158**, 107183 (2022).
15. N. Yoneda, Y. Saita, and T. Nomura, Opt. Lett. **45**, 3184 (2020).
16. N. Yoneda, Y. Saita, and T. Nomura, OSA Continuum **3**, 3523 (2020).
17. N. Yoneda, Y. Saita, and T. Nomura, Opt. Rev. **30**, 26 (2023).
18. V. H. F. Muñoz, N.-I. T. Arellano, D. I. S. García, A. M. García, G. R. Zurita, and L. G. Lechuga, Appl. Opt. **55**, 4047 (2016).
19. S. Aknoun, J. Savatier, P. Bon, F. Galland, L. Abdeladim, B. F. Wattellier, and S. Monneret, J. Biomed. Opt. **20**, 126009 (2015).
20. M. Takabayashi, H. Majeed, A. Kajdacsy-Balla, and G. Popescu, PLoS One **13**, e0194320 (2018).
21. W. J. Eldridge, A. Sheinfeld, M. T. Rinehart, and A. Wax, Opt. Lett. **41**, 352 (2016).
22. I. Choi, K. Lee, and Y. Park, Opt. Express **25**, 30771 (2017).
23. M. Tamamitsu, K. Toda, R. Horisaki, and T. Ideguchi, Opt. Lett. **44**, 3729 (2019).
24. K. Yamane, Z. Yang, Y. Toda, and R. Morita, New J. Phys. **16**, 053020 (2014).
25. G. Indebetouw, Y. Tada, and J. Leacock, Biomed. Eng. Online **5**, 63 (2006).
26. T. L. Nguyen, S. Pradeep, R. L. Judson-Torres, J. Reed, M. A. Teitell, and T. A. Zangle, ACS Nano **16**, 11516 (2022).
27. S. Shin, K. Lee, Y. Baek, and Y. Park, Phys. Rev. Appl. **9**, 044042 (2018).
28. S. Zhao, R. Liu, P. Zhang, H. Gao, and F. Li, Opt. Lett. **44**, 3278 (2019).
29. M. Li, L. Bian, G. Zheng, A. Maiden, Y. Liu, Y. Li, J. Suo, Q. Dai, and J. Zhang, Opt. Lett. **46**, 1624 (2021).
30. S. Kakei, K. Komuro, and T. Nomura, Appl. Opt. **59**, 2011 (2020).
31. T. Ito, K. Komuro, and T. Nomura, Appl. Opt. **60**, 4398 (2021).
32. N. Yoneda, Y. Saita, and T. Nomura, Opt. Express **30**, 18134 (2022).
33. J.-P. Liu, C.-H. Guo, W.-J. Hsiao, T.-C. Poon, and P. Tsang, Opt. Lett. **40**, 2366 (2015).
34. J.-P. Liu, Appl. Opt. **54**, A59 (2015).